ORNL/TM-2023/2839
NFE-21-08904

Electrically Engaged UnduLation (EEL) Marine Energy System

Vivek M. Rao, ORNL
John Turner, ORNL
Kevin Lu, Pyro-E LLC

August 2023

CRADA Final Report

OAK RIDGE National Laboratory

ORNL IS MANAGED BY UT-BATTELLE LLC FOR THE US DEPARTMENT OF ENERGY

DOCUMENT AVAILABILITY

Reports produced after January 1, 1996, are generally available free via OSTI.GOV.

Website www.osti.gov

Reports produced before January 1, 1996, may be purchased by members of the public from the following source:

National Technical Information Service
5285 Port Royal Road
Springfield, VA 22161
Telephone 703-605-6000 (1-800-553-6847)
TDD 703-487-4639
Fax 703-605-6900
E-mail info@ntis.gov
Website http://classic.ntis.gov/

Reports are available to US Department of Energy (DOE) employees, DOE contractors, Energy Technology Data Exchange representatives, and International Nuclear Information System representatives from the following source:

Office of Scientific and Technical Information
PO Box 62
Oak Ridge, TN 37831
Telephone 865-576-8401
Fax 865-576-5728
E-mail reports@osti.gov
Website https://www.osti.gov/

ORNL/TM-2023/2839

Water Power Technologies Office
Testing & Expertise for Marine Energy (TEAMER)

ELECTRICALLY ENGAGED UNDULATION (EEL) MARINE ENERGY SYSTEM

Vivek M. Rao
John Turner
Kevin Lu

August 2023

Prepared by
OAK RIDGE NATIONAL LABORATORY
Oak Ridge, TN 37831
managed by
UT-BATTELLE LLC
for the
US DEPARTMENT OF ENERGY
under contract DE-AC05-00OR22725

CONTENTS

LIST OF FIGURES

LIST OF TABLES

ACKNOWLEDGEMENT

The investigators would like to thank the U.S. Department of Energy for executing this study under CRADA# NFE-21-08904, the Nuclear Energy and Fuel Cycle Division at Oak Ridge National Laboratory for high-performance computing resources, and the Water Power Technologies Office for funding the investigation through the TEAMER program.

ABSTRACT

Current technologies at the forefront of instrumentation for ocean observation through acoustic mapping are powered by batteries that cannot achieve the lasting durations required for high-resolution measurements. Pyro-E has designed an Electrically Engaged unduLation (EEL) system capable of in situ energy harvest and deployment in sub-sea configurations. By extracting kinetic energy from the ocean, EEL proposes to provide power output ranging from 1 mW to 1,000 mW. Such a magnitude of power can sustain active instrumentation with onboard processing of data and over-the-horizon telemetry. Pyro-E and Oak Ridge National Laboratory have utilized software tools and powerful computing resources to develop a techno-economic design of the EEL capable of harvesting 5 W. The material response of the EEL under simulated hydromechanical loads is described through time-accurate predictions. All physical tests were conducted by Pyro-E to guide simulations at Oak Ridge National Laboratory.

1. INTRODUCTION

1.1 MOTIVATION

Through the US Department of Energy's Water Power Technologies Office's Testing and Expertise for Marine Energy (TEAMER) program, this project will develop a preliminary understanding of hydrodynamic responses by the Electrically Engaged unduLation (EEL) prototype toward the development of a 5 W marine power source to support seafaring devices for ocean observation by Pyro-E. Submersible swarms of EELs, as depicted in Figure 1, are proposed to make long-term ocean observation possible. Today, current ocean instruments powered by batteries lack the longevity to make persistent, wide-scale monitoring cost-effective. More specifically, the power consumption of the targeted battery instruments spans roughly three orders of magnitude from milliwatts to watts. These data platforms include types of ocean floats, buoys, and gravity-driven gliders. To power these systems, batteries must be replaced at sea, thereby requiring expensive labor for retrieval. If power is provisioned through energy harvesting, then full autonomy is achievable, including support for onboard processing and over-the-horizon telemetry. By bridging the gap of battery limitations, EEL aims to reduce the cost of ocean acoustic mapping through greater operational autonomy, spatial coverage, and temporal resolution.

1.2 ENERGY HARVESTING MECHANISM

The EEL ocean-observing system harvests hydrodynamic energy while maneuvering by mimicking the gait of aquatic eels. The flexible drone consists of a single-body submersible that can harvest energy from waves and currents. Power is generated during both station-keeping and depth profiling via the piezoelectric effect—a material-led phenomenon that converts applied stress into electricity. The key benefits include size, weight, volume, redundancy, and form. The targeted impact for EEL is to (1) mitigate battery limitation, (2) increase autonomy, and (3) reduce the cost of ocean data. The key innovations include the following features:

- Deployable at the ocean surface and at-depth
- Zero acoustic or chemical footprint
- Environmentally benign
- Power provisioning up to 5 W

Physically, EEL has a slender body the articulated spine of which is composed of energy units interconnected by flexible hinges. This design is visualized in Figure 2. Each unit consists of a pair of piezoelectric elements that convert the bending stress into electrical current to a battery charging circuit. An outer plastic skin forms a seal against water and allows flexibility at hinge locations. At the top is a bluff

body cylindrical head with electronics that holds a ballast for buoyancy adjustment. See Table 3 for component description. The bluff body is also responsible for creating the fluid instabilities in its wake. When moving through water, the spine flexes in response to the alternating vortices that shed from the head. The frequency at which vortices shed resonates with the EEL undulations to emulate the efficient gaits found in species of sea snake, eel, and fish. Ultimately, mimicking bio-locomotion provides a viable path to a self-propelled energy harvesting submersible for ocean monitoring. For the test article, only the energy harvesting components will be evaluated and not the buoyancy control. In further detail, EEL is a buoyancy-driven submersible glider with built-in energy harvesting for persistent operation at sea. The energy is generated from co-located energy sources associated with (1) surface waves or (2) hydrodynamic lift (i.e., during descent/ascent). A third mode uses a servo motor for active propulsion. Operationally, the power budget would include two modes of generation under various power usage activities estimated by Pyro-E, as shown in Table 1 and

Table 2.

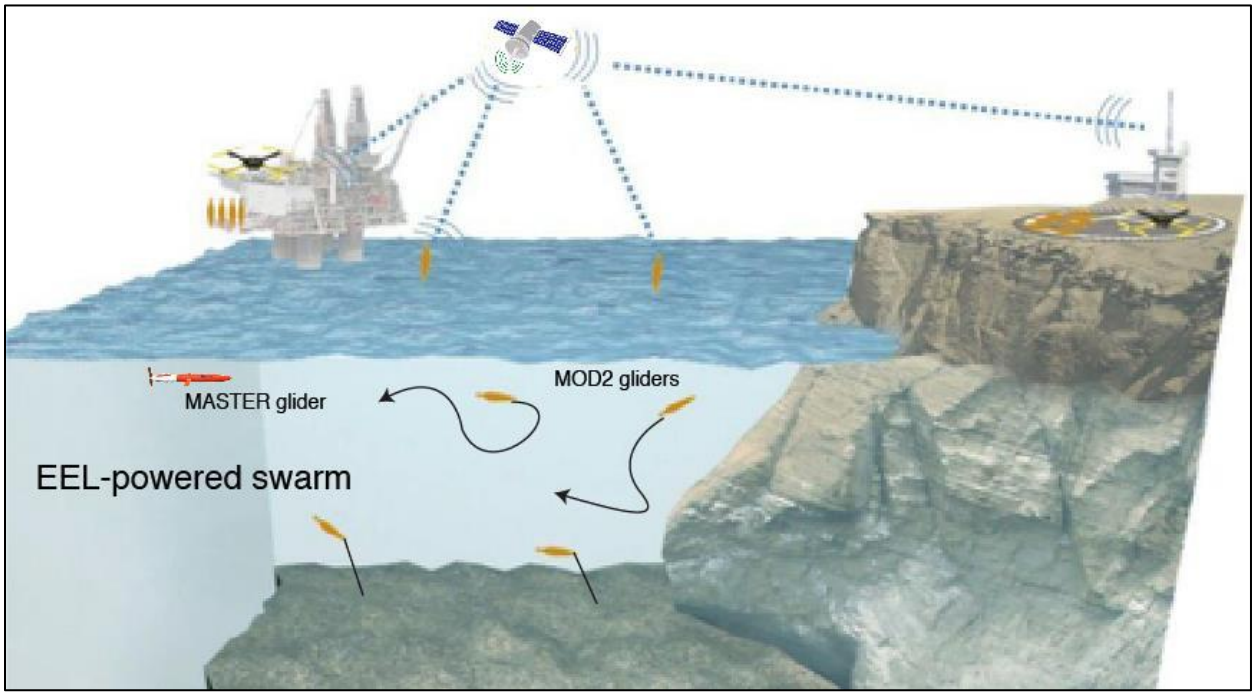

Figure 1. Proposed subsea swarm of EELs. Original artwork by Pyro-E.

Table 1. Projected Power Budget: Generation.

	Nominal Capacity	**% Duty Load**	**RMS Power**
Mode: Station-Keeping	8.19 W	20%	1.64 W
Mode: Passive Gliding	4.10 W	80%	3.28 W
Total Generation			**4.92 W**

Table 2. Projected Power Budget: Consumption.

	Nominal Capacity	% Duty Load	RMS Power
Mode: Station-Keeping	0.05 W	8%	0.004 W
Mode: Passive Gliding/Profiling	1.0 W	90%	0.9
Mode: Active Propulsion	185 W	2%	3.70 W
Navigation & Control	0.1 W	100%	0.1
Sampling & Data	0.1 W	85%	0.085 W
Communication	1.5 W	5%	0.075 W
Total Consumption			**4.86 W**
Net Power			**0.052 W**

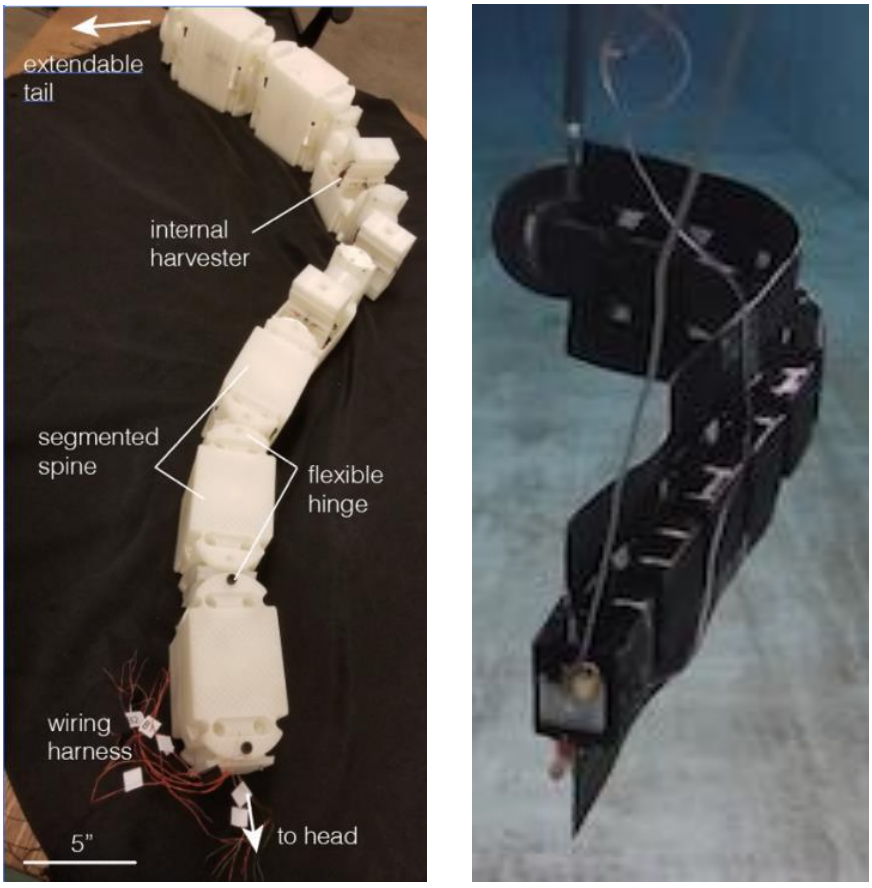

Figure 2. EEL prototype – piezoelectric core (L) and operating test shroud (R).

1.3 FUNCTIONAL DEVELOPMENT OF EEL PROTOTYPE

Within the EEL prototype shown in Figure 2, the components serve distinct purposes. The next section describes the function, geometry, material and anticipated dry mass of each component as proposed by Pyro-E.

1.3.1 Head

Function: The head is a neutrally buoyant bluff body. The frontal area of the head will be designed to generate instabilities in the streamlines, such as alternating vortices around the bulk body and corresponding forces.
Geometry: The head will be a cylindrical, bullet-like structure with faring and flow control fins.
Material: Acrylic plastic with O-ring seals and an internal proof mass for buoyancy.
Dry Mass: 9.4 kg (21 lb).

1.3.2 Tail

Function: The tail will provide hydrodynamic efficiency to EEL with articulated body segments containing internal compartments and lateral fins. The fins are proposed to provide a higher lift-to-drag ratio.
Geometry: The external dimensions (L, W, H) are proposed at 2 m × 0.1 m × 0.05 m. The length and lift will be adjustable.
Material: Stainless steel for body segments and nylon 66 skin for water seal.
Dry Mass: 14 kg (31 lb).

1.3.3 Hinge

Function: Hinges will provide a single-axis rotation mechanism to render flexibility to the tail.
Geometry: Ball-in-socket design with adjustable bending stiffness.
Material: Steel ball and nylon socket.
Dry Mass: N/A.

1.3.4 Energy-Harvesting Core

Function: Pressure-sensitive materials with compliant epoxy coatings will be used to harvest energy from the flow field.
Geometry: The core will be embedded into tail compartments. Approximately, 100 pressure-sensitive elements will comprise the energy-harvesting core.
Material: Multi-layered ceramic, with a compliant amplifier mechanism.
Dry Mass: 200 g.

1.3.5 Electronics

Function: The on-board electronics will manage power with up to 48 piezo-inputs and battery storage.
Geometry: A 4 in. × 6 in. printed circuit board (PCB) and a lithium-ion storage for the battery will provide 500 mAh of operation.
Material: Analog power chipsets will be used for durability and low-power operation.
Dry Mass: 100 g.

2. OBJECTIVES

2.1 PHYSICAL TESTING OF EEL PROTOTYPE

Pyro-E is in the process of gathering experimental data through measured and visualized oscillation profiles in a tow tank facility at the Stevens Institute of Technology. Pyro-E also has led the analysis of materials and the method of electric power generation. No validation data are discussed in this document. Pyro-E will use the findings from numerical simulations discussed in this document to inform the sizing of the EEL

prototype and to conduct further testing based on the analyses of fluid–structure interactions (tail displacements) and the generated thrust profiles.

2.1.1 Test Metrics for EEL Prototype

The goal for Pyro-E is to achieve a hull design that maximizes performance across the three modes of operation: gliding/profiling, station-keeping, and active propulsion. The design is motivated by bio-locomotion such that EEL mimics the efficient gait of slender-body animals for swimming. Remarkably, it has been observed that fish species such as salmon can exhibit passive propulsion against the flow—which may explain how the animal rests behind rocks to reach upstream freshwater during the spawning season. Therefore, the proposed objectives focus on emulating the fluid–structural coupling of animal species for energy harvesting while reducing drag. Details include:

- Objective 1: Confirm 500% higher wetted surface area to device mass.
- Objective 2: Confirm 25% drag force reduction from equivalent hard-shelled gliders.
- Objective 3: Confirm net root means square (RMS) generation greater than 3 W with varying operating modes and duty.

Table 3. Targets proposed for EEL prototype by Pyro-E.

Operating Mode	Metric	Proposed Practice
Station-keeping	Hydrodynamic efficiency	> 85%
Passive gliding	Total drag	25% reduction
Combined modes	Net generation	> 3 W
Active propulsion	Speed	> 6 knots

2.2 HYDRODYNAMIC SIMULATION OF EEL PROTOTYPE

To achieve test performance targets for the EEL prototype, the prescribed simulations aim to capture the time-accurate response of the EEL prototype under the operating modes of station-keeping, passive gliding, and active gliding. To accomplish this, the simultaneous effects of essential physical phenomena must be considered. Primary interactions arise from wave periodicity at the free surface (air–water interface) on the wetted walls of the EEL prototype, the conversion of incident pressure into electricity through piezoelectric materials, and the effect of the tail oscillations on the ambient flow field. It is expected from simpler examples that the effect of hydrostatic pressure on the wetted walls will be consistently dominant, and locally in the flow field, the effect of the tail oscillations will be significant on the flow field. High spatial resolution of these physical phenomena in time is achieved using pertinent models in STAR-CCM+. Descriptions are provided in the following subsections. All equations are executed in finite-volume formulations within respective models. *Stipulated conditions for simulations are replicated from test conditions set by Pyro-E in units of ft/s. Therefore, boundary conditions are input in ft/s, not m/s, to avoid input error. All computed quantities are reported in S.I. units.*

2.2.1 Air–Water Interface and Wave Physics

Operation of the EEL prototype aims to power ocean observation activities and equipment. Therefore, the ideal test environment for simulation is the free surface of water bodies. In this control volume, wave physics are mathematically discretized using two models in the Eulerian volume of fluid (VOF) approach—namely, the VOF model and the VOF waves model. The VOF model is based on a high-resolution interface capturing algorithm [1] which is formulated to track the interface between immiscible, Eulerian fluid phases. Therefore, it is important to maintain sufficient mesh resolution over the sampling course of

simulations. Additionally, the resolution of interfaces can be sharpened by accounting for slip between the phases. The transport equation for phase volume fraction is given by

$$\frac{\partial}{\partial t}\int_V \alpha_i dV + \oint_A \alpha_i \boldsymbol{v}.d\boldsymbol{a} = \int_V (S_{\alpha_i} - \frac{\alpha_i}{\rho_i}\frac{D\rho_i}{Dt})dV - \int_V \frac{1}{\rho_i}\nabla.(\alpha_i\rho_i\boldsymbol{v}_{d,i})dV .$$

The equation for continuity of air and water phases is given by

$$\frac{\partial}{\partial t}\int_V \rho\boldsymbol{v}dV + \oint_A \rho\boldsymbol{v}.d\boldsymbol{a} = \int_V SdV.$$

Where S is the mass source term that is related to the phase source terms by

$$S = \sum_i S_{\alpha_i}\rho_i.$$

The equation for the momentum of the air-water mixture is given by

$$\frac{\partial}{\partial t}\int_V \rho\boldsymbol{v}dV + \oint_A \rho\boldsymbol{v}\times\boldsymbol{v}.d\boldsymbol{a} = \oint_A p\boldsymbol{I}.d\boldsymbol{a} + \oint_A \boldsymbol{T}.d\boldsymbol{a} + \int_V \rho g dV + \int_V f_b dV - \sum_i \int_A \alpha_i\rho_i\boldsymbol{v}_i ,$$

where p is the pressure, I is the unit tensor, T is the stress tensor, and f_b is the vector of body forces.

Since the flow is assumed to be incompressible, conservation of energy is not considered. More detail on the high-resolution interface capture algorithm is available in the work of Muzaferija and Peric [2].

The VOF waves model uses the captured interface between immiscible phases to simulate surface gravity waves. Various types of waves (flat, Stokes waves, Cnoidal, irregular) can be simulated with the VOF waves model. In this study, a first-order wave is used. Here, the wave is modeled as a first-order approximation of the Stokes theory of waves. The generated wave has a regular sinusoidal profile. Other relations are listed below.

Wave velocity: $v_v = a\omega\sin(K.x - \omega t)\, e^{Kz}$

Surface elevation: $\eta = \text{acos}\,(Kx - \omega t)$

Wave period:

$$T = \frac{2\pi}{\lambda}$$

Wave length:

$$\lambda = \frac{2\pi}{K}$$

Dispersion relation between period and length of a first order wave in water of depth, d:

$$T = \left[\frac{g}{2\pi\lambda}\tanh\left(\frac{2\pi d}{\lambda}\right)\right]^{-1/2}$$

These models are well suited to study of the hydrodynamic response of the EEL prototype to various wave perturbations in station-keeping mode. Pyro-E has provided wave conditions within which the EEL

prototype is proposed to operate; they are listed in the table below. It should be noted that the parameters specified in Table 4 by Pyro-E are the wave period (T) and wave height (H). The wave height is twice the wave amplitude. In STAR-CCM+, the wave height cannot be used as an input, but wave amplitude can, and it is used in the simulations as half the incoming wave height.

Table 4. Station-Keeping Modes and Excitation Regimes.

	H = 0.05 m	**H = 0.1 m**	**H = 0.2 m**	**H = 0.4 m**	**H = 0.8 m**	**H = 1.6 m**
T = 1 s	Small Excitation	Medium Excitation			Large Excitation	
T = 3 s						
T = 9 s						

In this mode, EEL will be submerged at a shallow depth below the free surface of water. The kinetic energy of subsurface currents is to be harvested by EEL at depths up to a few meters and converted to electric current. In simulations, it is assumed that this depth is less than 2 m. To represent ambient waves and resulting excitation in a representative domain, the conditions listed in Table 4 are used.

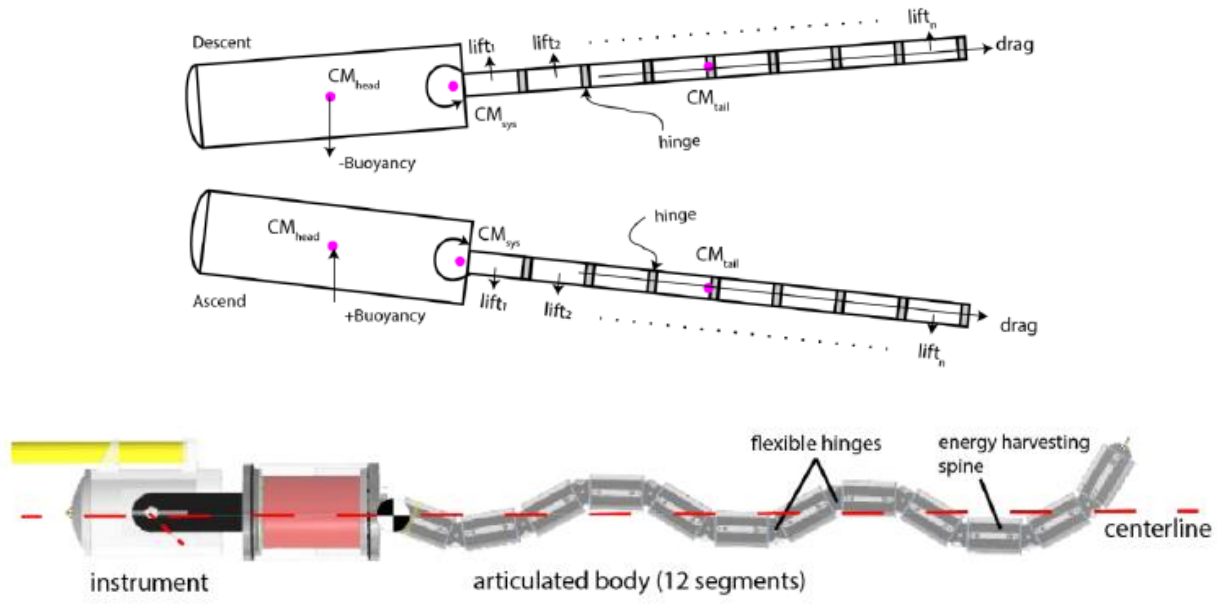

Figure 3. Hydrodynamic forces acting on EEL prototype, proposed by Pyro-E.

Preliminary study by Pyro-E with low-fidelity coupled fluid structural simulations using Ansys Mechanical/Fluent were conducted for the preliminary design parameters of EEL. The approach taken is a fluid structure coupled analysis using dynamic meshing. Results were obtained on the range of Reynolds (RE) to validate meshing and stability over 3 s. However, large deflections were not captured by this method. Such regimes would be required for the "lock-in" conditions, definable through published results:

- $1200 < Re < 15000$, which determines the laminar and turbulent modes of excitation
- $0.15 < St < 0.25$, which determines resonant and off-resonant modes of excitation
- $4 < MR < 8$, which determines the bluff body dimension for optimum excitation

Improved fidelity modeling will help validate the parametric model to streamline optimization and better predict product performance. A representative image of the expected simulation result is attached. Overall, the hydrodynamic regimes are resonant, non-resonant, laminar, and turbulent modes. By matching published data, the goal of numerical modeling is to delineate the EEL regimes under which EEL synchronizes with the shedding vortices of the bluff body and whose interaction becomes the most efficient.

2.2.2 Turbulent Flow

Turbulence in the mixture of immiscible fluid phases is approximated by solving a closure formulation of the Reynolds-Averaged Navier–Stokes (RANS) equations using the Realizable k-ε Turbulence model and the Two-Layer y+ Wall Treatment model. By decomposing each solution variable to the Navier–Stokes equation into an averaged component and a fluctuating component, ensemble averaging is performed for transient simulations. Thus, the equations of transport for averaged mass and averaged momentum can be given by

$$\frac{\partial \rho}{\partial t} + \nabla \cdot (\rho \bar{v}) = 0 ,$$

$$\frac{\partial \rho(\bar{v})}{\partial t} + \nabla \cdot (\rho \bar{v} \otimes \bar{v}) = -\nabla \cdot \bar{p}\,\mathbf{I} + \nabla \cdot (\bar{T} + T_{RANS}) + f_b,$$

where ρ is the density, $\bar{v}$ is the mean velocity, $\bar{p}$ is the mean pressure, **I** is the identity tensor, f_b is the total of body forces, and $\bar{T}$ is the mean viscous stress tensor.

Much like the transport equations for the original scalar variable, the new equation set differs by the addition of T_{RANS}, which is defined as

$$T_{RANS} = -\rho \begin{pmatrix} \overline{u'u'} & \overline{v'u'} & \overline{w'u'} \\ \overline{u'v'} & \overline{v'v} & \overline{w'v'} \\ \overline{u'w'} & \overline{v'w'} & \overline{w'w'} \end{pmatrix} + \frac{2}{3} \rho k \mathbf{I} .$$

To model T_{RANS} as a function of mean flow quantities, an eddy–viscosity approach is used based on the Boussinesq approximation. This further involves solving for the turbulent viscosity, or eddy viscosity, which provides an analogy between the molecular diffusion–scale transport and the turbulent, eddy-scale transport,

$$T_{RANS} = 2\mu_t \boldsymbol{S} - \frac{2}{3}(\mu_t \nabla \cdot \bar{v})\mathbf{I} ,$$

where *S* is the mean strain rate tensor.

In this study, the Realizable k-ε model uses two additional equations of transport for turbulent kinetic energy (k) and the turbulent dissipation rate (ε) to solve for the turbulent viscosity (μ_t). The Realizable k-ε model employs the low–Reynolds number approach to calculate μ_t by splitting the solution into two layers next to domain walls. In the wall-adjacent layer, ε and μ_t are empirically specified as a function of distance from the wall. In the second layer, the values of ε are interpolated with the calculated values away from the two near-wall layers. Then, *k* is solved for across all cells. The theoretical formulation was adapted from the work of Shih et al. [3] and uses a damping function to satisfy realizability constraints for the normal stresses. This approach has been validated in literature when simulating similar, free-surface flows around ships [4] and is well suited to this study. It is suggested that the model shows good agreement for wall coordinate y+ ~ 1 in the low–Reynolds number approach, or at y+ > 30, outside the viscous sublayer. Accordingly, the y+ > 30 has been maintained in this study to avoid field adaption sensitivity for dynamic meshing and to keep the global cell count low for computational affordability.

2.2.3 Fluid–Structure Interaction (FSI)

The dynamism of the EEL prototype is expected to arise from the coupling of kinematic consistencies between the fluid and the solid domains. The fluid transfers pressure and wall shear stress data to the solid at the fluid–solid interface. Similarly, the solid sequentially transfers deformation data to the fluid. This is known as two-way fluid–structure interaction (FSI) coupling. Further complexity arises in this study from rigid body motion of individual tail segments, with rotation of segment pairs at contacting hinges, and translation of rigid bodies along the Cartesian coordinates. To resolve rigid body motion, the dynamic fluid–body interaction (DFBI) framework must be concurrently applied. To further model stresses in the solid, the Flexible DFBI Motion model must be enabled. Under this model, a partially deformable DFBI body mode can then be enabled in the solid domain. This allows the EEL prototype to move rigidly in response to the ambient forces of flow and deform locally under sufficient force from the fluid subject to the provided thermomechanical properties. In a two-way FSI problem, topological consistency is maintained by the vertices in fluid volume, which morph for conformity with the deformed solid structure and vice versa using the arbitrary Lagrangian–Eulerian technique. In STAR-CCM+, the 6DoF Mesh Morpher solver employs a radial basis to define the new locations of morphing vertices. Therefore, care must be taken to prevent drastic depreciation of cell quality in morphed cells. This is overcome using an overset mesh and mapping at the contact interface(s).

2.2.4 Overset Mesh Strategy

During the FSI simulation, the re-organization and re-sizing of cells as a result of morphing must be accommodated by fixed gaps in the solid walls. Cells in the fluid will expand or contract depending on eccentric motion, of the solid away from its original state. Therefore, an overlap in the overset volumes is intentionally created to prevent excessive squeezing or expansion of cells in the fluid volume. This approach is demonstrated by the following steps:

- The CAD model is fully developed to isolate the final, solid volumes/bodies.

- A background volume is created where the wave and air–water phases will exist over the life of the simulation.

- Overset volumes are created around each solid body for specificity. A single volume can contain multiple solid bodies. Ideally, each overset volume can clearly create segregation between solid bodies that are mere obstacles to flow and remain static and solid bodies that will move rigidly and/or deform under fluid stresses. Static solid bodies may simply be subtracted from the background volume if no solid stress data are desired therefrom.

- The overset volumes are allowed to overlap to accommodate cells that will create a buffer and prevent excessive expansion or compression of fluid cells during the morphing stage.

- The domains are then separated into background, overset, and solid regions. Each region can further be moved or be kept stationary. Overset boundaries are assigned to the exterior walls of the overset fluid volumes. Then, overset interfaces are created between overlapping overset volumes (one per overlap) and between each overset volume and the background volume. Lastly, a fluid–solid contact interface is created between the deformable solid body/bodies and the corresponding overset volume (static wall(s)).

3. DESIGN STRATEGY AND PRELIMINARY ANALYSIS

3.1 ITERATIVE DESIGN DEVELOPMENT

3.1.1 Segments: 0, Tail: 1

3.1.1.1 *EEL Orientation for Vertical Oscillation:* A simplified CAD model of the EEL prototype was previously developed by Pyro-E to estimate a high-level overview of hydrodynamic responses using computational fluid dynamics (CFD) software. In this model, the fore of the EEL is designed as a rectangular block with a hemispherical head. The tail is a flexible rectangular strip. Both bodies were assumed to be fabricated from polyethylene. This model was tested at 1D ambient flow speeds of 2 m/s and 3 m/s, as suggested by Pyro-E. As a simple test, this showed that the model could generate a monotonically increasing tail oscillation, as seen in Figure 4, which reaches an observed steady amplitude after the initial startup. The oscillation amplitude remains steady over a simulated period of 30 s and is suggested to last as such under a steady inflow of wave energy.

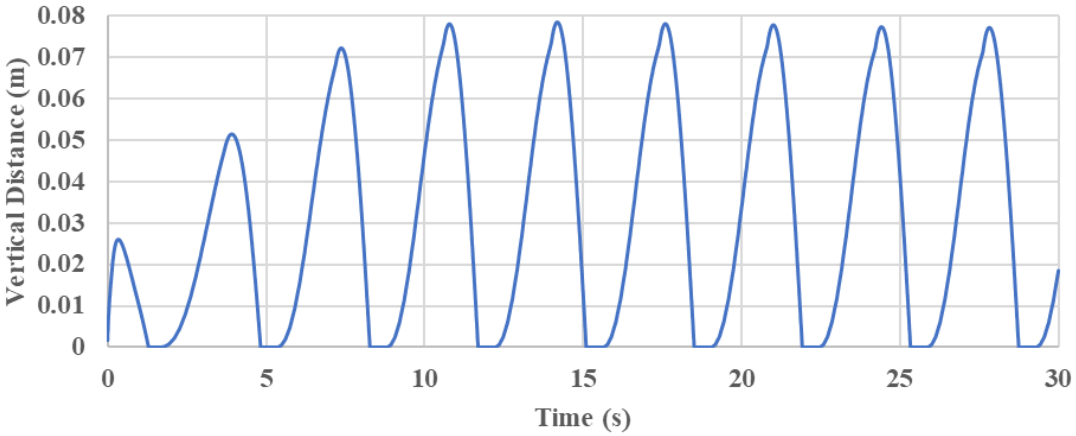

Figure 4. History of vertical oscillation of EEL tail over 30 s of simulated time.

Figure 5 shows the deformation (displacement) produced by fluid–solid interactions; it also shows velocity fields (magnitude, radial) at 30 s of simulated time. The combined force of pressure and shear force on the wetted wall manifests as an equivalent mechanical force resulting in surface undulations.

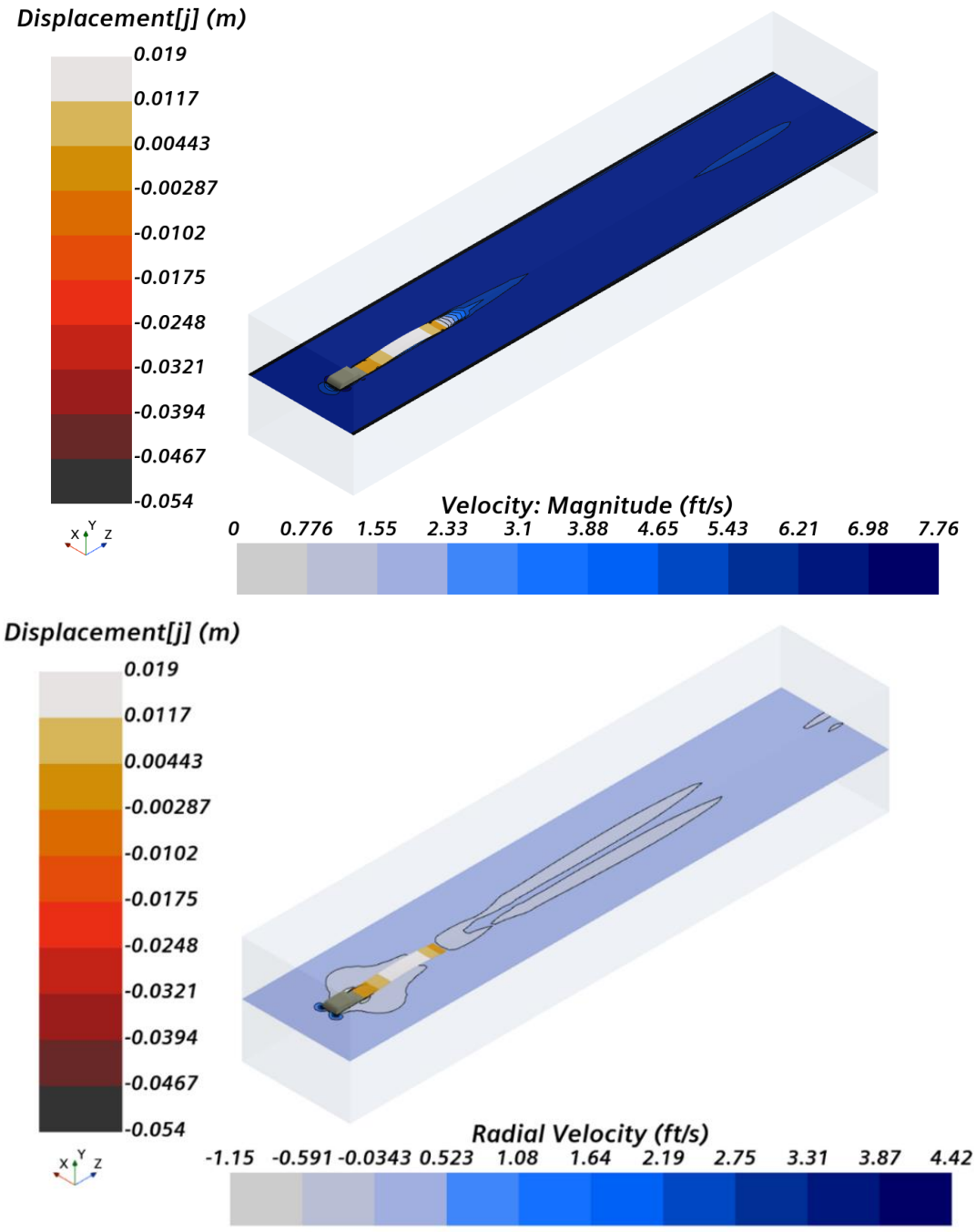

Figure 5. Segments, Tail (0,1): hydrodynamic response to ambient flow field of 6 ft/s.

3.1.1.2 EEL Orientation for Horizontal Oscillation: The settings used for the solvers were retained and applied to a horizontal orientation to assess magnitudes of displacement, that is, more harnessed power.

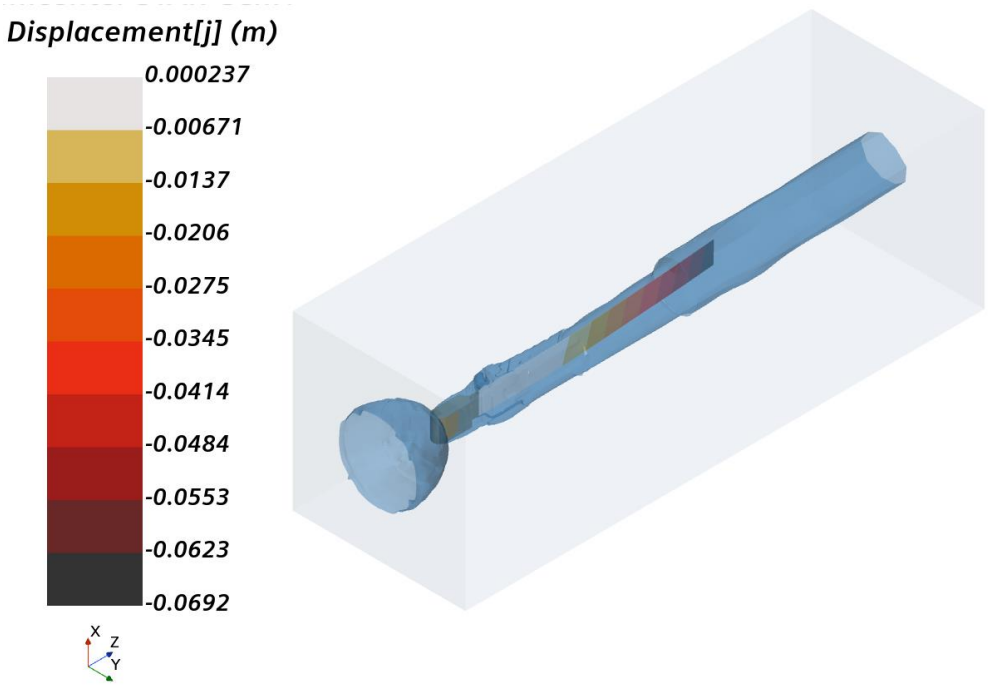

(a) Iso-surface of 2 m/s flow around EEL prototype

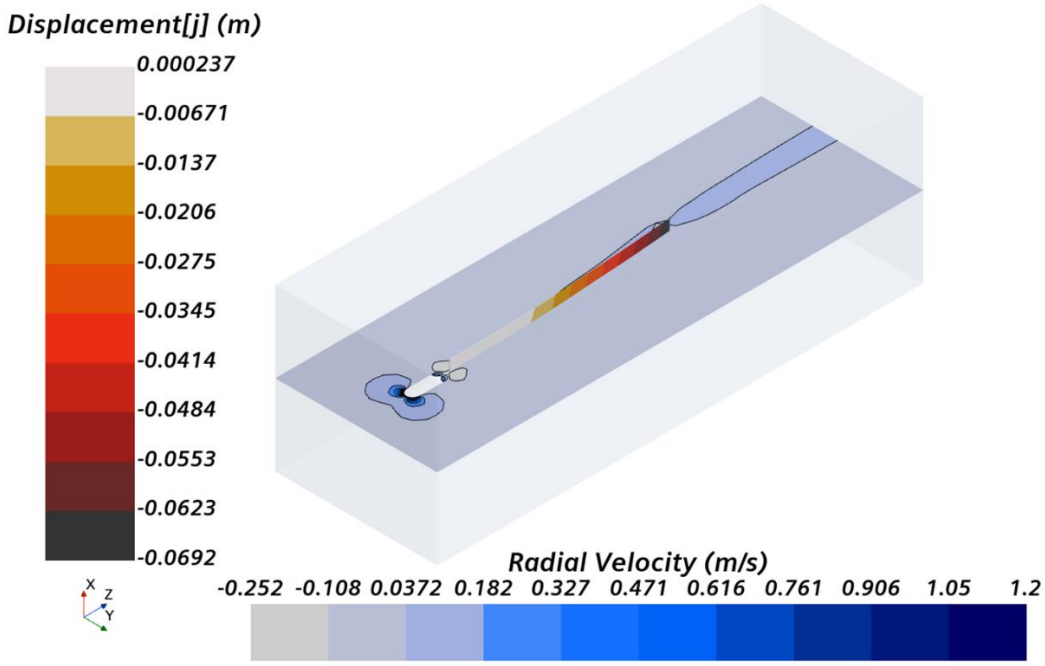

(b) Radial velocity contours normal to the cross-section of the tail

Figure 6. Horizontal displacement of EEL prototype under ambient flow of 2 m/s.

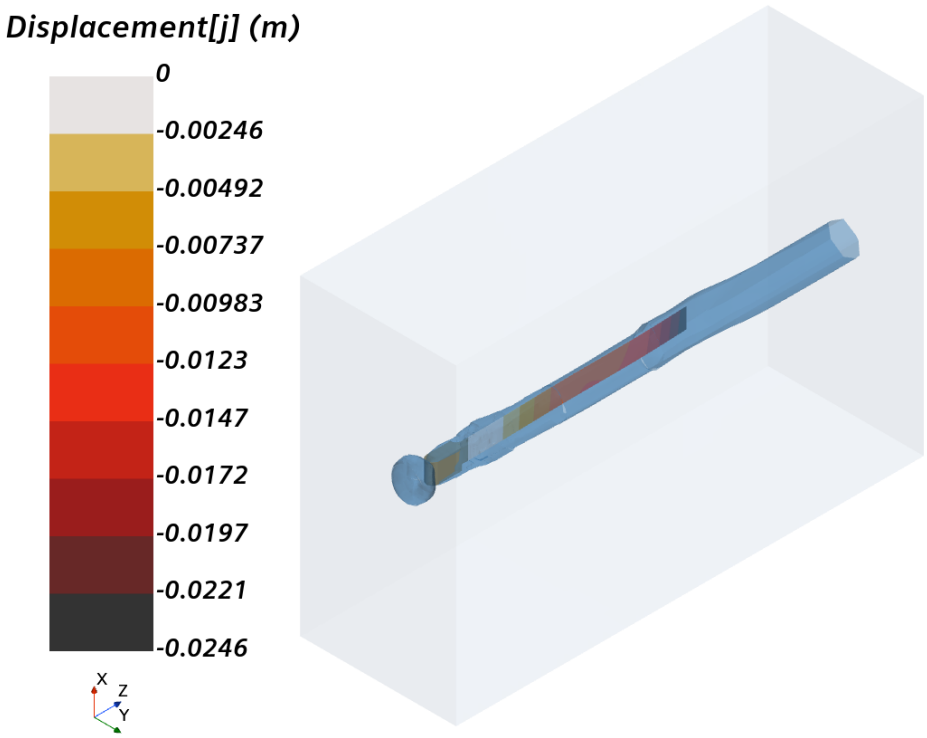

(a) Iso-surface of 3 m/s flow around EEL prototype

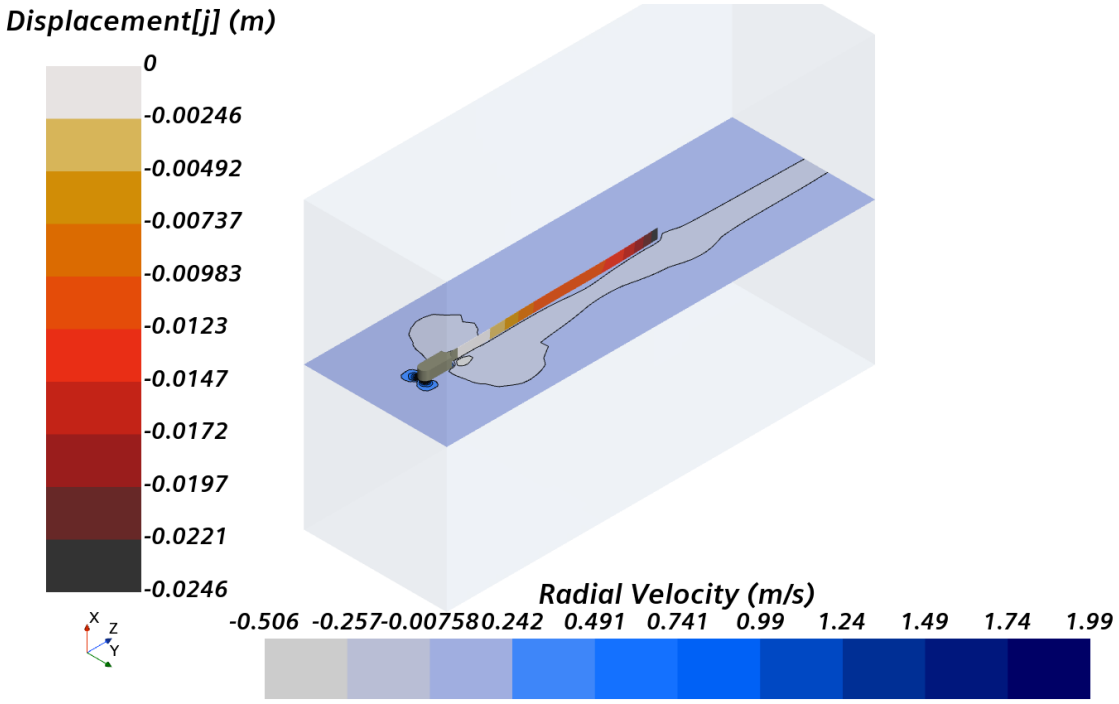

(b) Radial velocity contours normal to the cross section of the tail

Figure 7. Horizontal displacement of EEL tail under ambient flow of 3 m/s.

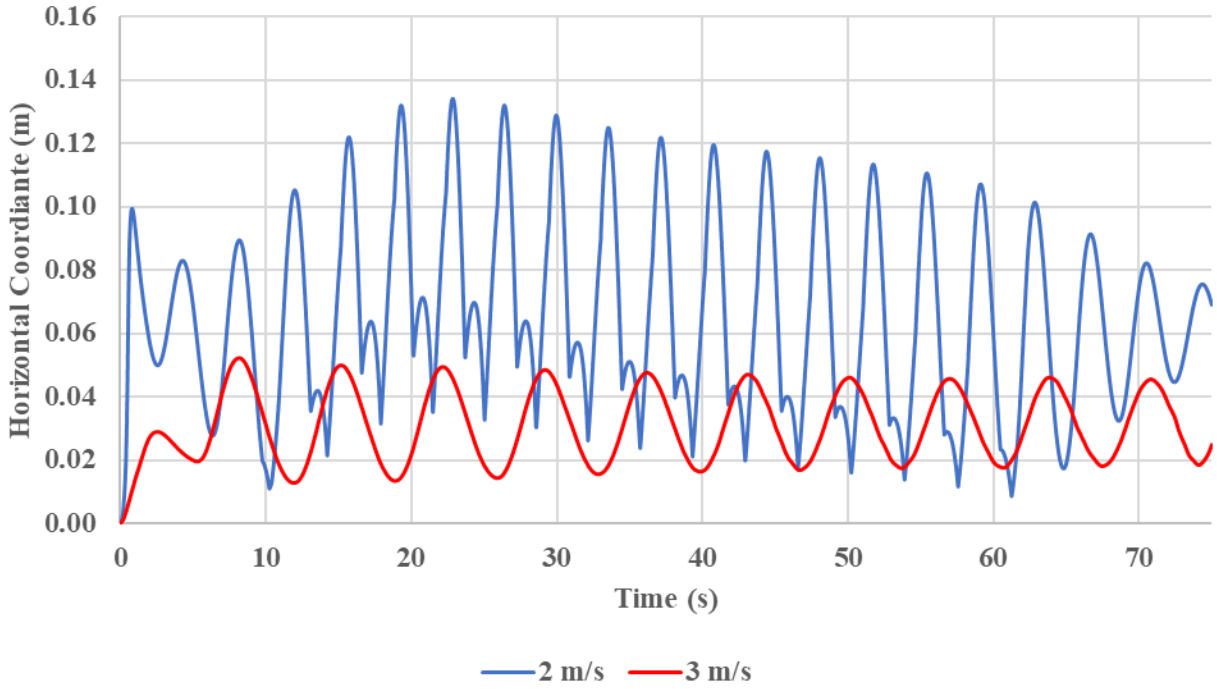

Figure 8. History of horizontal tail oscillations over 75 s of simulated time.

From the observed trends in Sec. 3.1.1.1 and Sec. 3.1.1.2, it was inferred that the horizontal orientation induced larger deformations in the simplified tail representation and provided computational efficiency to guide the setup of the true CAD model developed by Pyro-E for the EEL prototype. The computational design of the EEL prototype is described in detail in the Sec. 3.1.2.

3.1.2 Segments: 10, Tail: 1

In this design, the fore of EEL is represented by a two-part head (polymer fore, head body), ten piezoelectric segments, and a tail body. Choice of materials is controlled by Pyro-E. A tail body was introduced to provide a smooth wake downstream of the piezoelectric segments. The first piezoelectric segment is connected to the head, the last piezoelectric segment is connected to the tail, and each pair of piezoelectric segments are connected by hinges. For brevity, the ten piezoelectric segments are referred to hereinafter simply as *segments*. *Tail* refers to the tail body downstream of the tenth piezoelectric segment. Hinges are represented by revolute joints in the simulation and are treated as massless bodies placed in the exact locations of hinges in the EEL test prototype.

By using the actual masses of the head and segment from the test prototype, simulations were run to study the oscillation profile created by the head and tail of the EEL prototype. These profiles were tracked over 75 s of simulated time at ambient flow speeds of 6 ft/s and 10 ft/s. For stability of the prototype in simulated flow, it was assumed that the head body was immovable. In a real application, this would represent the forces of anchoring or towing. It was also assumed that the EEL prototype is in submerged water. Therefore, there is no air influencing the flow field. With the enabled Flexible DFBI model in Star-CCM, the bodies were expected to exhibit a combination of local deformation due to solid stresses from interaction with the fluid, as well as rigid body motion.

3.1.2.1 *EEL Orientation for Vertical Oscillation:* A preliminary comparison of this design was tested, once again, in vertical and horizontal orientations. Simulation of EEL in a vertical orientation showed good mobility of the flexible segments but poor mobility for the tail. The segments

showed minimal deformation along the vertical axis but notable physical rotation about the hinges. A deeper investigation into the tail body showed that the peak displacement induced by solid stresses was insufficient to deform the tail (peak displacement lower than 1 mm) and benefit from a 'flapping' motion of the tail; for this phenomenon, sufficient mechanical force would have to be relayed through the segments and hinges towards the tail to generate sufficient deformation.

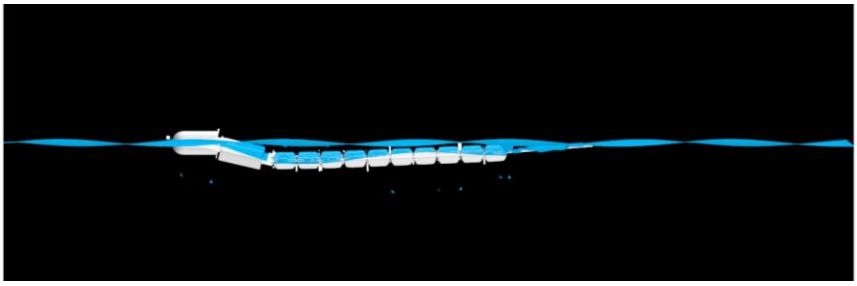

(a) EEL in motion: tail near free surface, segments and head submerged

(b) EEL tail exhibiting low flexibility with peak solid displacement less than 1 mm

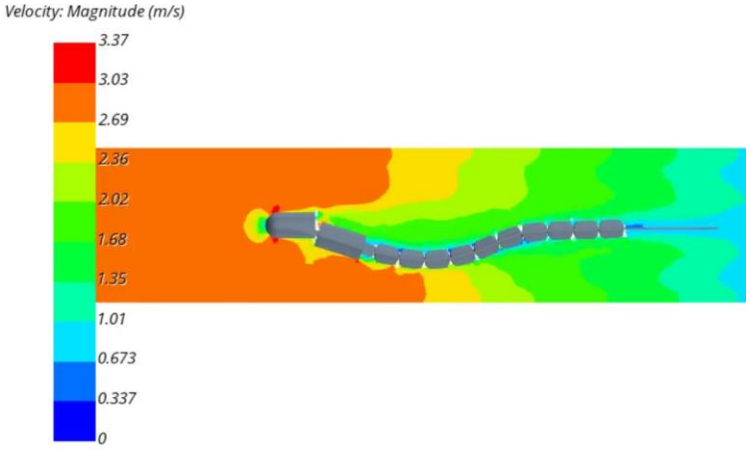

(c) Velocity field around EEL showing high velocity flow at curved surfaces of the head body

Figure 9. EEL design in vertical orientation.

3.1.2.2 EEL Orientation for Horizontal Oscillation: In a horizontal orientation, EEL performed noticeably better in terms of qualitative agreement with test observations, as well as agreement with quantitative displacements of similar magnitude. This comparison is shown in Figure 10.

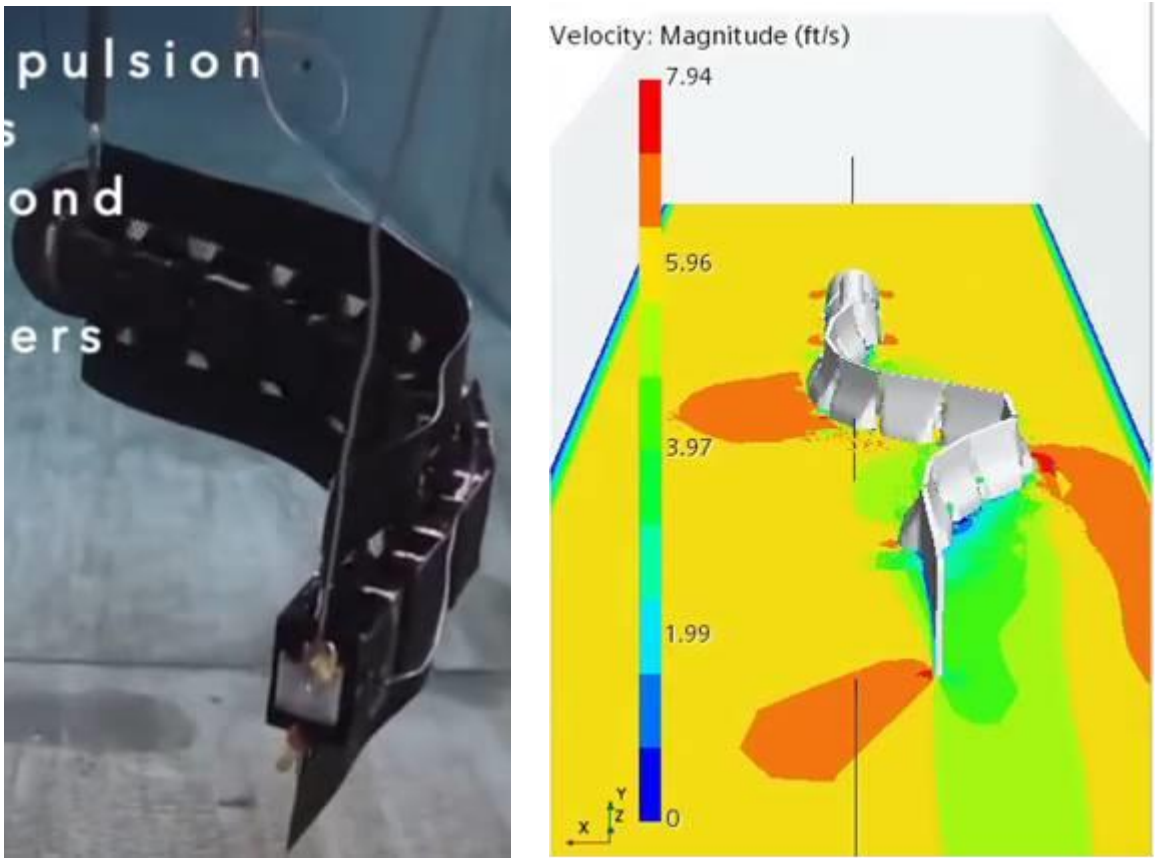

Figure 10. A comparison of hydrodynamic response for EEL between test and simulation.

Despite larger oscillations of the EEL segments and tail intially away from the prototype centerline, the tail was once again found to exhibit unfavorable stiffness. This stiffness once again led to numerical instabilities due to unphysical forces enacted at the segments, creating unphysical flow fields due to fluid–solid interactions. From these results, the trajectory of the tail suggested that the relative motions of piezoelectric segments do not allow the tail to ascribe to a net, pure oscillatory motion. Instead, both simulations show intermittency in the oscillations but do not repeat to establish a steady oscillation. The reports of thrust, however, were useful in indicating the difference between the lift force (vertical) and the fluid forces (lateral) generated by the fluid on wetted walls.

Two salient inferences were made based on continued, detailed simulations with this design.

- EEL suffers a crumpling effect owing to the stiffness of the tail: there is rigid, axial motion of the tail and segments toward the fixed head. Numerically, this effect does not resolve itself and leads to immediate instability in simulations.

- Flexibility of the tail body can be partially improved by choosing a material of Young's modulus lower than 1e8 Pa , but this alteration is not sufficient to significantly improve the oscillation height of the EEL prototype overall; therefore, a design without a tail would be more cost-feasible.

Therefore, the tail was removed, and the number of segments was increased to 15. This model is described in the next section.

3.1.3 Segments: 15, Tail: 0

This design was tested in the horizontal orientation only since it was found in Sec. 3.1.2.2 and in Sec. 3.1.1.2 that the horizontal orientation was more favorable for larger oscillations. Furthermore, long-term simulations show favorable "lock-in" conditions [4] i.e., suitable amplitudes of oscillation for tested mass of EEL specimen without inducing fatigue in the material, at ambient flow velocities of 10 ft/s. Therefore, this design was tested in the horizontal orientation under test conditions of 6 ft/s and 10 ft/s. Initial analyses showed qualitative agreement between the EEL test prototype and the predicted shape from simulations. An example from the simulation is provided in Figure 11.

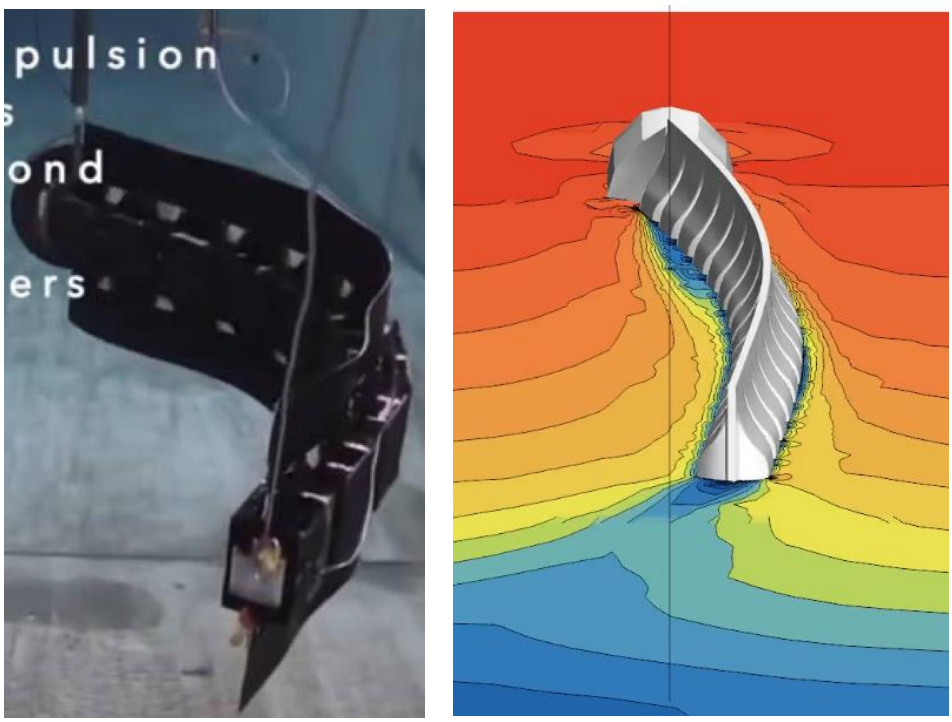

Figure 11. A comparison of qualitative response for EEL between test and simulation.

Based on this initial qualitative agreement, this design was selected to study station-keeping and passive gliding modes for operating modes prescribed by Pyro-E. Video animations of this EEL design reaching lock-in conditions in submerged conditions were generated and assessed by Pyro-E for concurrence prior to continuing the study.

4. FINAL DESIGN, RESULTS, AND ANALYSIS

4.1 STATION-KEEPING MODE

The combinations of wave height and wave period described in Table 4 were each run to simulate the hydrodynamic response of the EEL design developed in Sec. 3.1.3. The following figures describe the history of thrust generated on the wetted walls of the EEL design. Figure 12 to Figure 14 provide the lateral thrust generated by EEL due to fluid–solid interactions, whereas Figure 15 to Figure 17 provide the axial

thrust or lift force generated on EEL, due to vertical forces exerted on the smaller fin-like cross section area of EEL by ambient water.

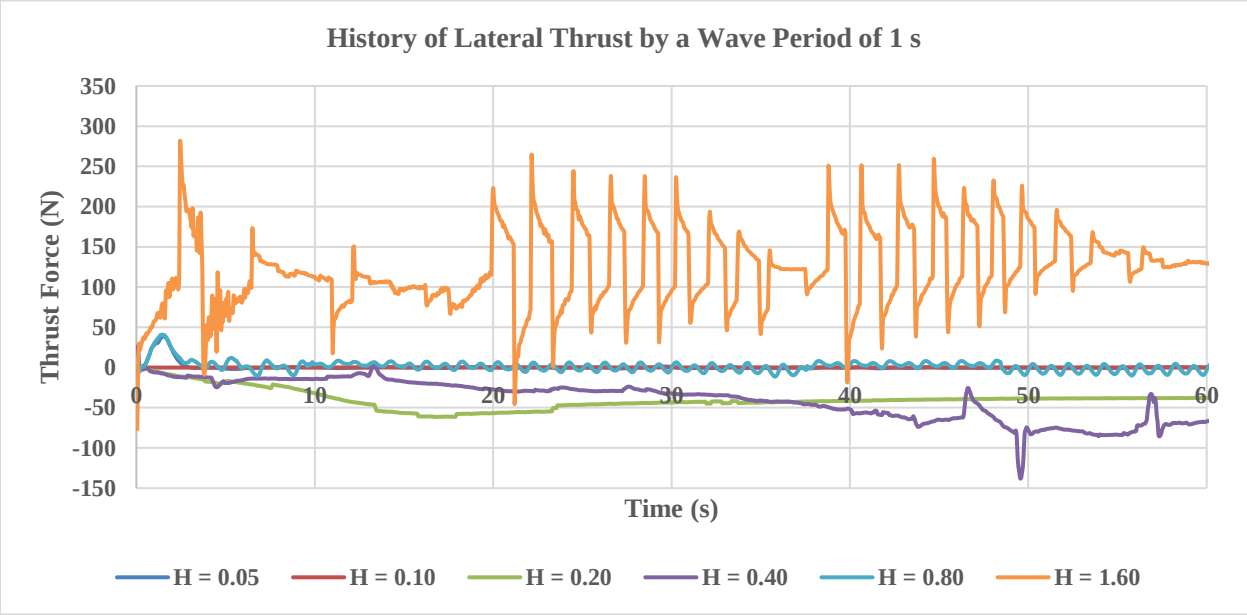

Figure 12. History of lateral thrust generated for a wave period of 1 s.

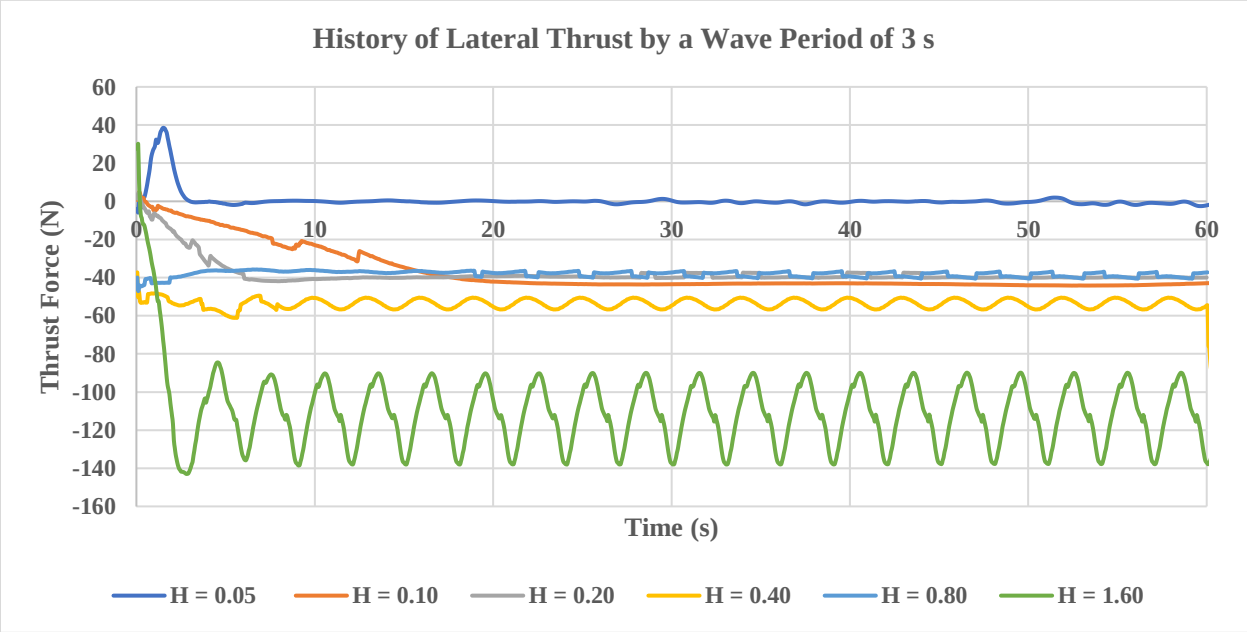

Figure 13. History of lateral thrust generated for a wave period of 3 s.

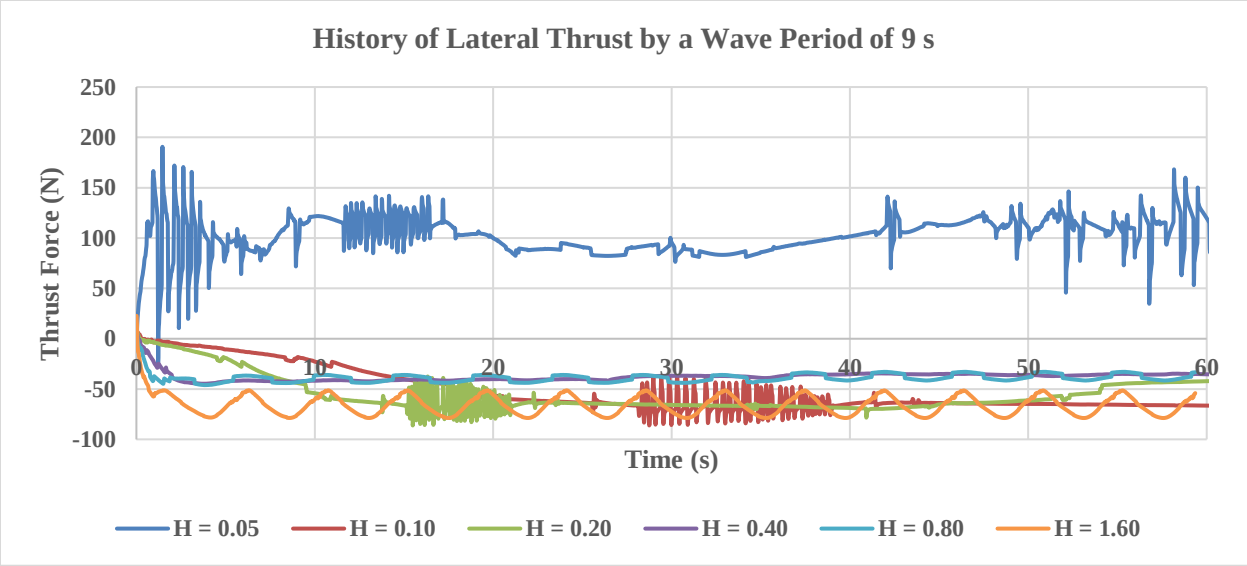

Figure 14. History of lateral thrust generated for a wave period of 9 s.

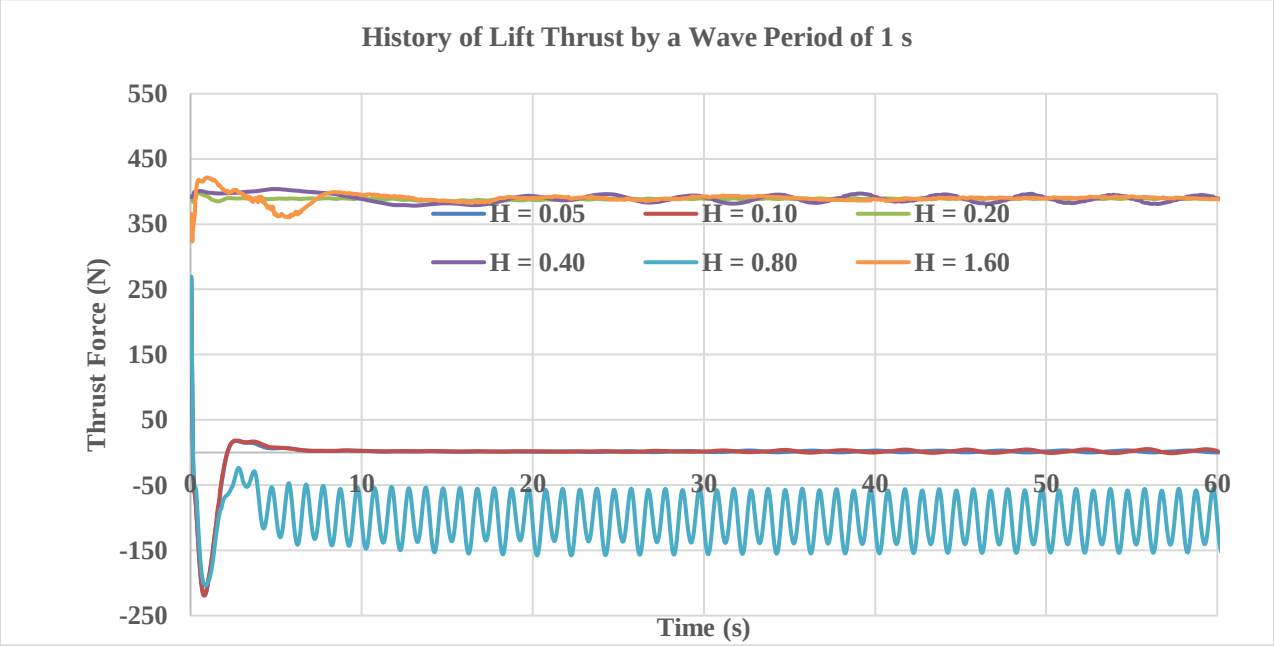

Figure 15. History of lift generated for a wave period of 1 s.

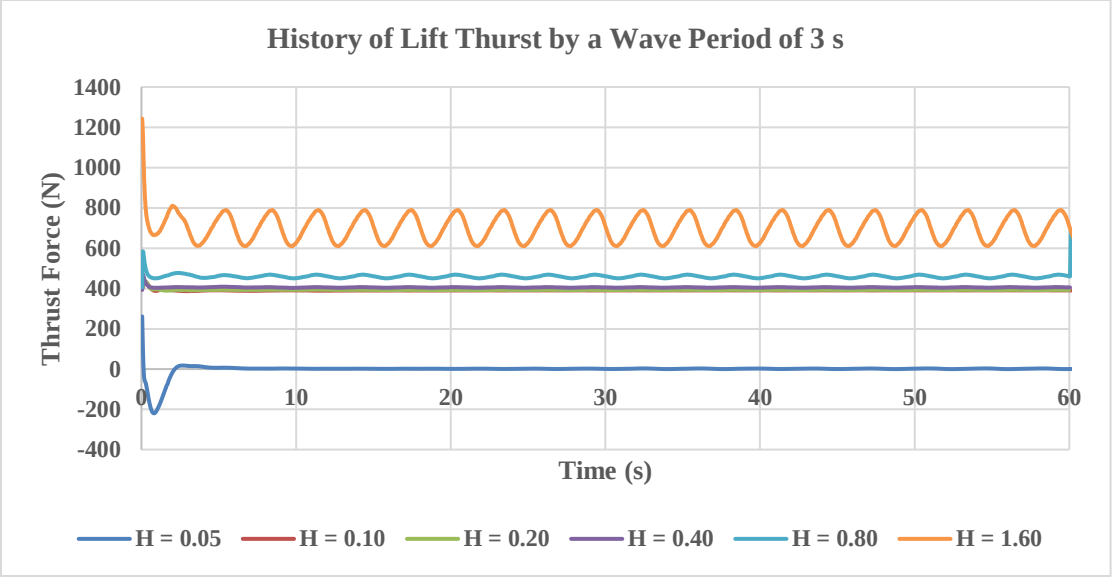

Figure 16. History of lift generated by a wave period of 3 s.

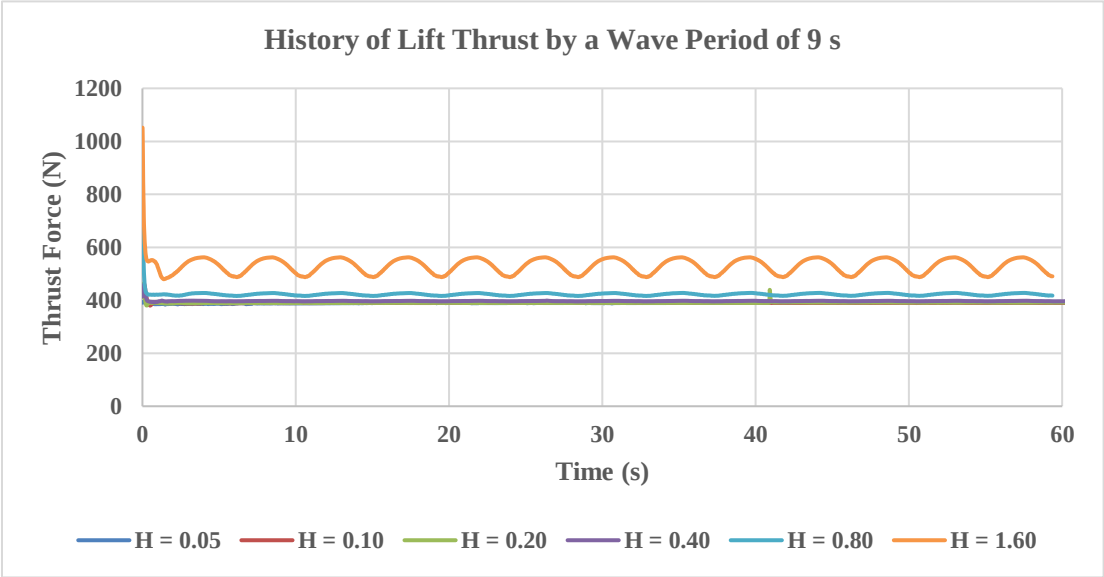

Figure 17. History of lift generated by a wave period of 9 s.

At first observation, the largest lateral thrust is achieved at a wave period of 1 s and a wave height of 1.60 m. The thrust profile generated in Figure 12 over 60 s shows three cycles of a similar pattern: the peak thrust generated deteriorates before starting over. This is suggested to correspond with cascading turbulent kinetic energy in the local flow field with time. It should be noted that at a wave height of 0.80 m, the lock-in condition is observed, but the magnitude of thrust generated is significantly lower. Of the tested wave periods, a thrust force of value during lock-in condition is manifested by recorded lateral thrust for a wave period of only 3 s and a wave height of 1.60 m. Here, the EEL tail shows consistent, repetitive profiles over 60 s and produces reliable lateral thrust under unchanging wave profiles. At a wave period of 9 s, this lock-in condition is observed once again at the largest tested wave height of 1.60 m, but the magnitude of lateral thrust produced is notably lower than that during a wave period of

3 s. The lowest lateral thrust profile is achieved during a wave period of 1 s and a wave height of 0.05 m. It was further concluded that tail displacement profiles would proportionately follow the same qualitative trends as those of the corresponding thrust profiles. This result is consistent with the proposed excitation to the EEL prototype based on preliminary analysis conducted by Pyro-E.

4.1.1 Passive Gliding Mode

In passive gliding mode, the EEL design would be towed by a secondary source of energy and would harvest any energy from fluid forces. With resonant, non-resonant, laminar, and turbulent regimes suggested by Pyro-E, it was decided that studying the hydrodynamic response of EEL in submerged conditions under velocities of 6 ft/s and 10 ft/s were of interest for design development. Pyro-E had already completed a test tow of the EEL prototype at the time at a velocity of 3 ft/s. Therefore, ambient flow velocities of 3 ft/s, 6 ft/s, and 10 ft/s were selected for simulation. The total mass of the device was estimated at 15 kg. Variations in total mass to 30 kg and 7.5 kg were also studied under the influence of ambient flow fields. The objective of this analysis was to identify the flow conditions or range thereof that provide maximum lateral thrust and optimum axial thrust based on tracked displacements of the tail. Although thrust profiles could be directly compared, it is essential to provide displacement data for the tail corresponding to the mass of the prototype so that Pyro-E can validate these predictions during tow tests.

As expected, each simulated scenario initially produces an oscillating response of EEL to perturbation in the flow field from an initially stagnant flow. From Figure 18 through Figure 20, it is seen that of the tested ambient velocities, at 3 ft/s and 6 ft/s, the whipping of tail commences over the first 45 s before reaching a quasi-steady state. This state represents finite yet insignificant oscillations that are of no favorable value to the EEL performance. However, under an ambient velocity field of 10 ft/s, the whipping motion follows a monotonically increasing value until the frequency and oscillation height reach a noticeably steady value. Notably, the lateral oscillations of all three masses at an ambient flow of 10 ft/s are of interest and represent oscillation heights of 80–90 cm (7.5 kg, 15 kg) and 100 cm (30 kg). This suggests that the scale of inertia for a prototype mass of 30 kg is similar to the inertial scale of turbulent stresses in the proximal flow field. Between 6 ft/s and 10 ft/s, the inertia of the prototype is marginally overcome by the flow field, and the effect of wall shear stress and pressure together create a monotonically increasing whip action. Figure 21 through Figure 23 compare the lateral tail displacement history for different tail masses at ambient velocities of 3 ft/s, 6 ft/s and 10 ft/s. Figure 24 through Figure 26 compare the axial displacement of the tail for tested velocities at a fixed mass of 7.5 kg, 15 kg, and 30 kg.

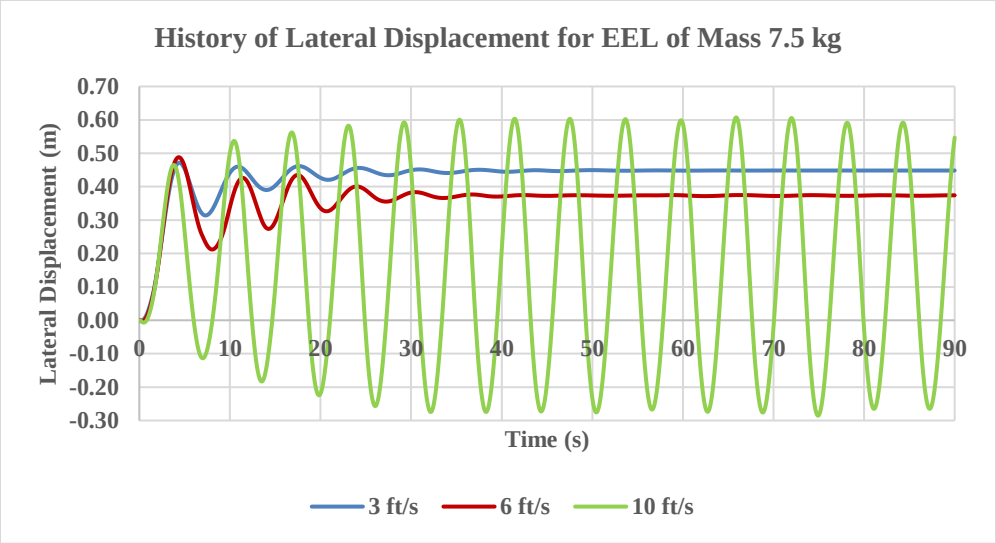

Figure 18. EEL tail displacement, *lateral*, for prototype mass 7.5 kg.

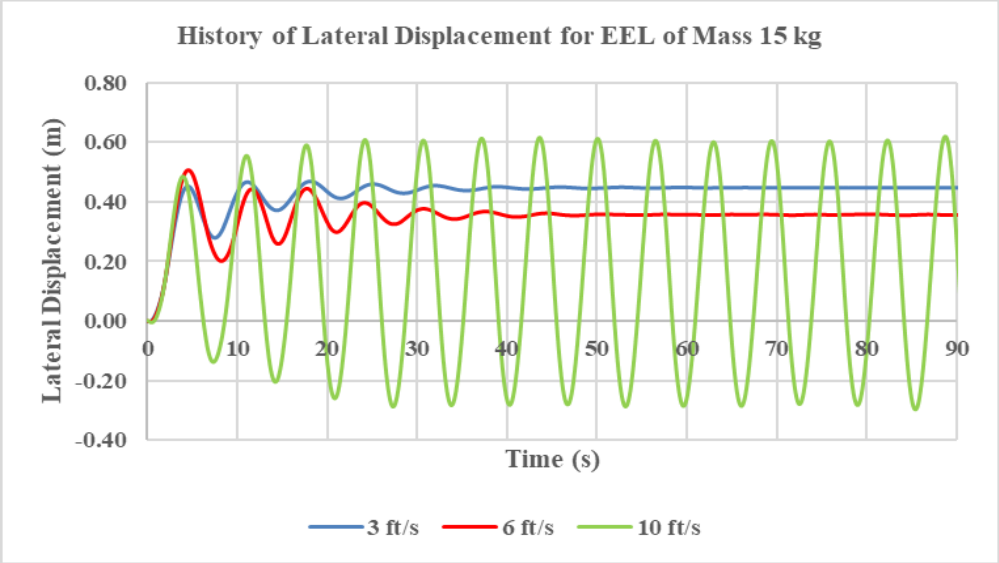

Figure 19. EEL tail displacement, *lateral*, for prototype mass 15 kg.

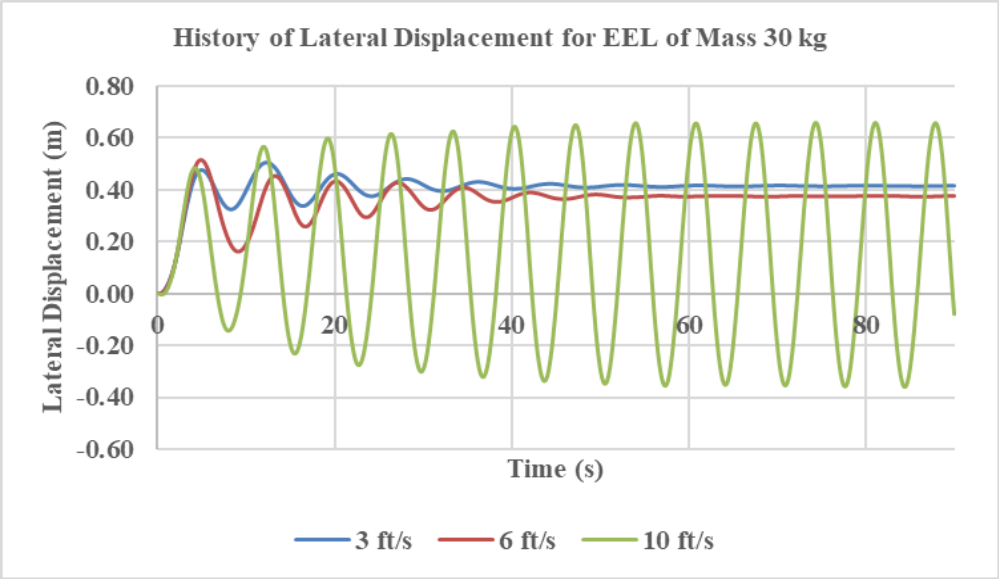

Figure 20. EEL tail displacement, *lateral*, for prototype mass 30 kg.

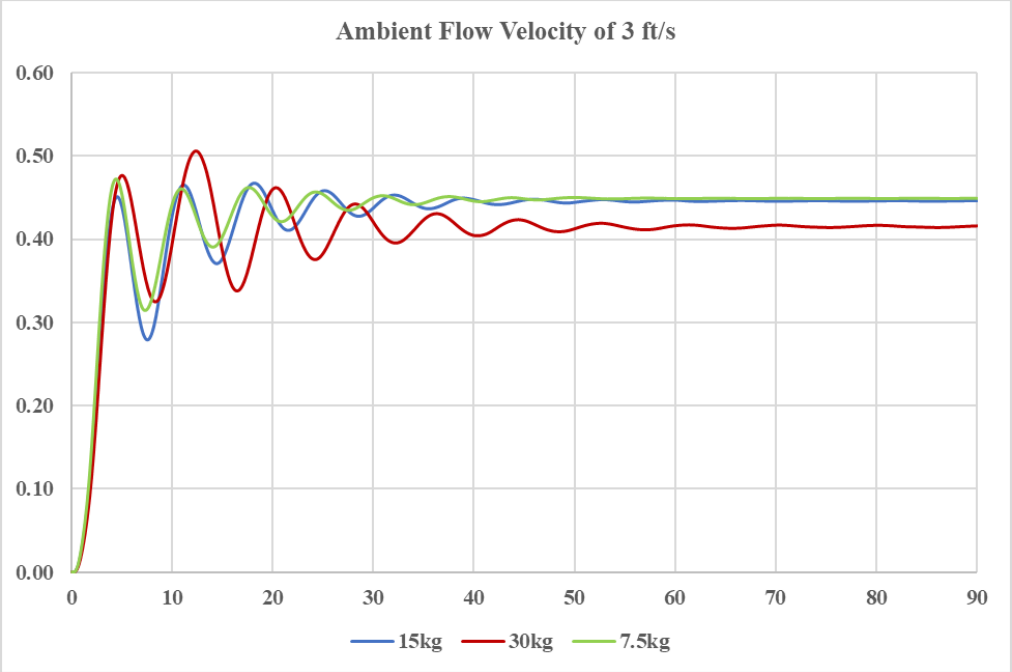

Figure 21. EEL tail displacement, *lateral*, for varied prototype masses at U = 3 ft/s

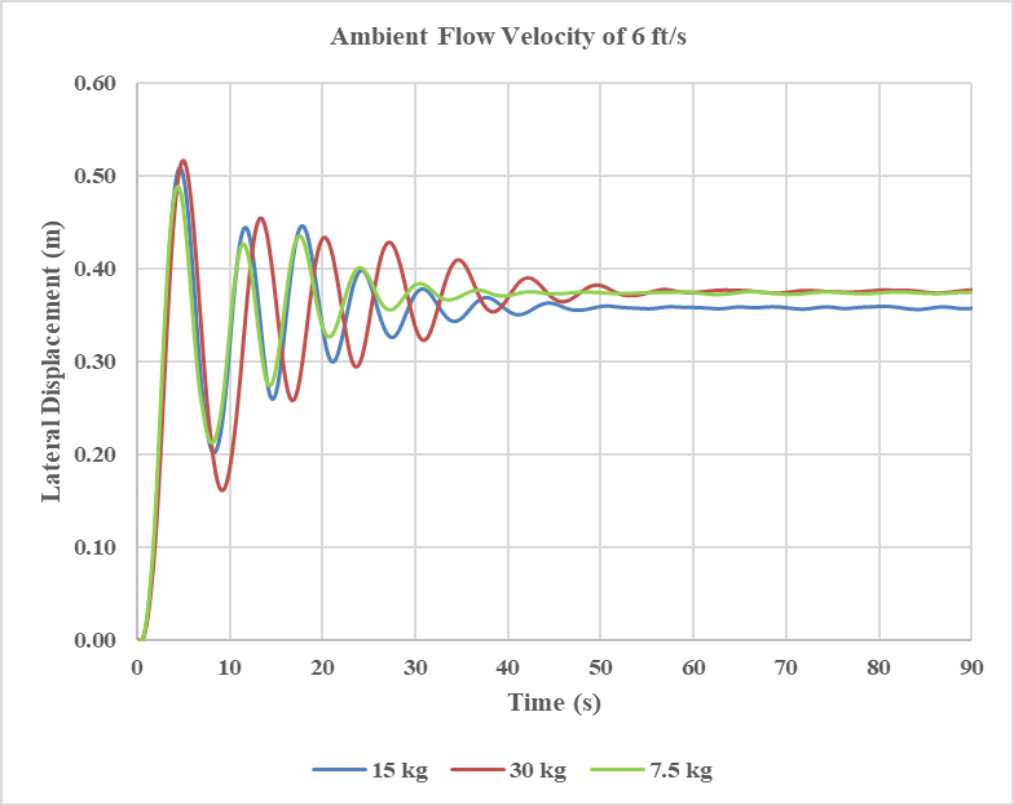

Figure 22. EEL tail displacement, *lateral*, for varied prototype masses at U = 6 ft/s.

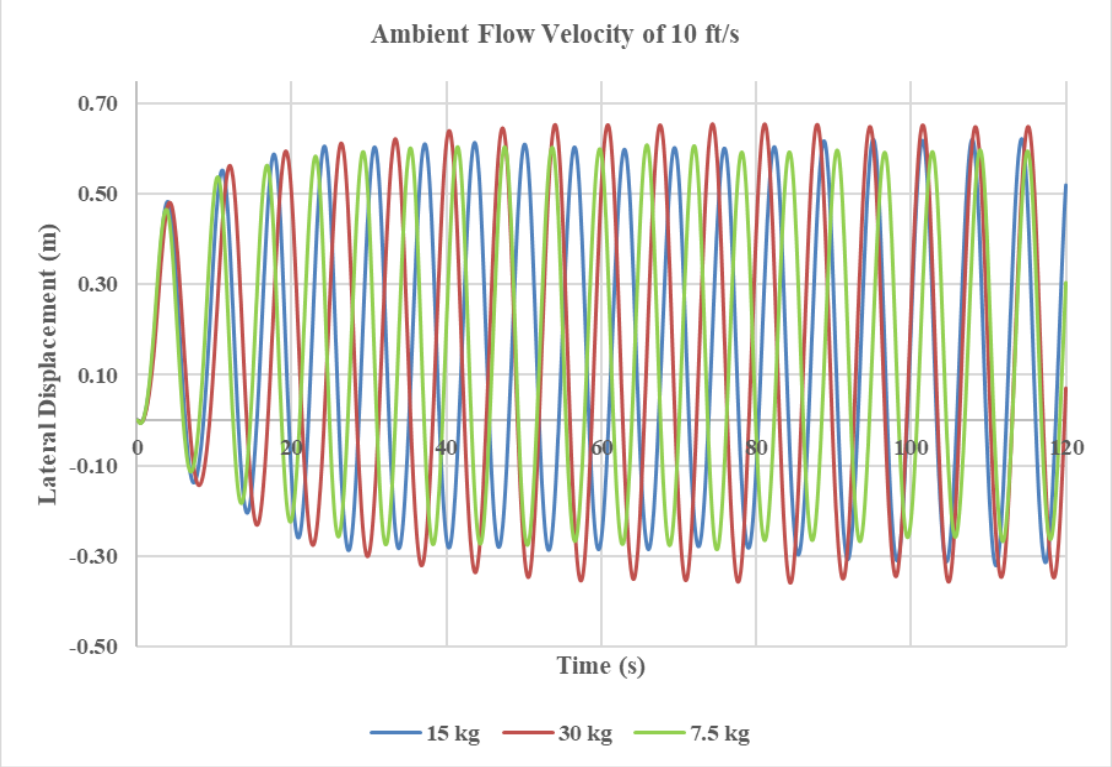

Figure 23. EEL tail displacement, *lateral*, for varied prototype masses at U = 10 ft/s.

Figure 24. EEL tail displacement, *axial*, for prototype mass 7.5 kg.

Figure 25. EEL tail displacement, *axial*, for prototype mass 15 kg.

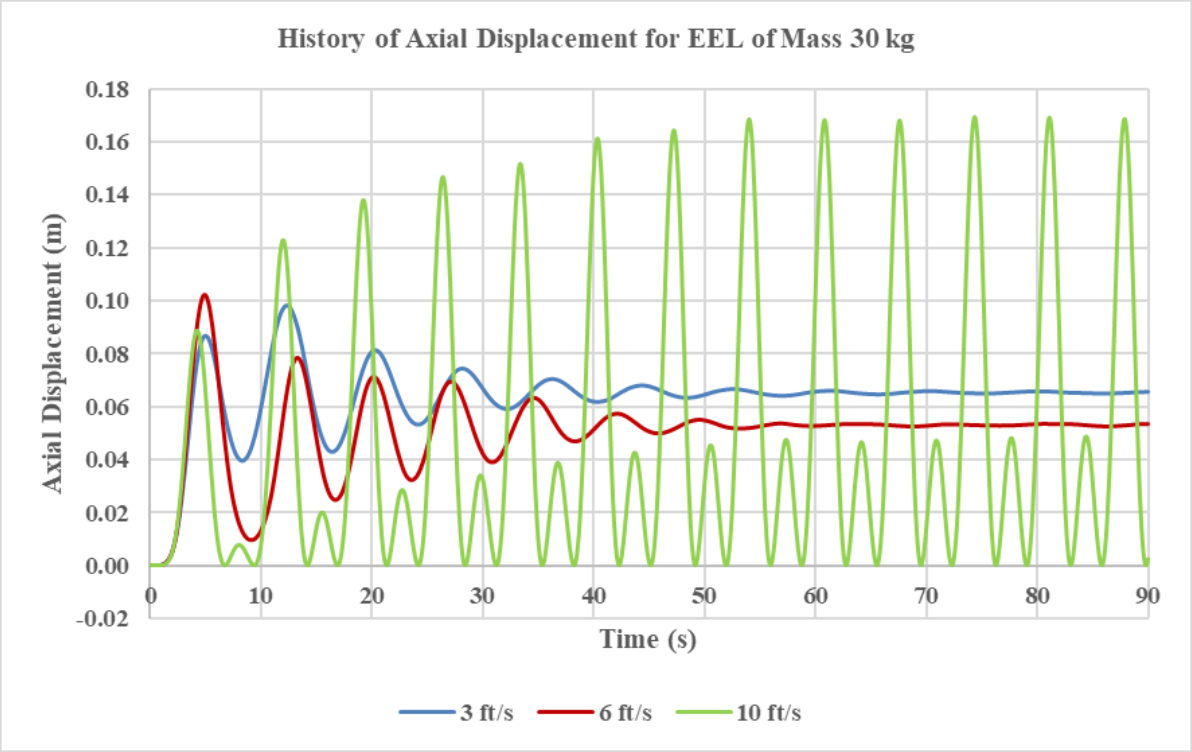

Figure 26. EEL tail displacement, *axial*, for prototype mass 30 kg.

Figure 21 and Figure 22 show that at 3 ft/s and 6 ft/s the mass of the prototype does not create a significant difference to the steady-state profile, that is, the mean value of displacement about which the tail oscillates. It can be observed that at 3 ft/s the prototype of mass 30 kg reaches a mean value approximately 4 cm lower than those of mass 7.5 kg and 15 kg. However, the amplitude of individual oscillations is higher for the mass of 30 kg than for 7.5 kg and 15 kg. This behavior is similarly exhibited at ambient flow of 6 ft/s. However, at 10 ft/s, the ambient flow produces a lock-in oscillation for all three prototype masses—once again supporting the argument that between 6 ft/s and 10 ft/s sufficient force of flow is achieved to overcome the inertia of the prototype and induce lock-in oscillations. Although the quantitative displacements of the prototype tails are of similar value in the first few seconds, by 120 s of simulation, the greater masses exhibit greater heights of oscillation. At 30 kg, the prototype tail produces an oscillation estimated at a little over 100 cm (1 m), 92 cm at 15 kg, and 83 cm at 7.5 kg. For a startup transient of less than 120 s, the response of the prototype is well suited for commercial development.

Though not of primary importance, the axial displacement of the tail in horizontal orientation due to lift forces in the vertical direction are essential to understand. Figure 24 through Figure 26 suggest that axial displacements of the EEL prototype under a fixed ambient velocity increase with mass of the prototype. Also, an ambient velocity of 10 ft/s is the only scenario to produce large, favorable oscillations for all three prototype masses: 14 cm (7.5 kg), 15.25 cm (15 kg), and 16.75 cm (30 kg). Video animations provided to Pyro-E provide further detail into the dynamic combination of axial and lateral displacements under the tested ambient velocities.

4.1.2 Active Propulsion Mode

In the simulation setup, a thrust force can be added to the passive gliding scenario. Once testing data are available at Pyro-E, analysts can simply add a value for thrust force from testing to simulate an active gliding scenario. The converted electric force will be used to propel the EEL prototype. Therefore, it is

difficult to estimate *a priori* how much force can dynamically be applied in the CFD study to estimate active gliding. This will be a welcome scope for future work.

5. CONCLUSIONS

An EEL prototype was developed by Pyro-E to establish a device that can support long-term ocean observation efforts through marine energy. Through the TEAMER program at the US Department of Energy's Water Power Technologies Office, Pyro-E and Oak Ridge National Laboratory investigated through computational tools and high-performance computing resources the hydrodynamic response of EEL prototype designs under various flow scenarios common to ocean waves. Pyro-E provided Oak Ridge National Laboratory a basic design of the EEL prototype and a set of tests to be simulated at prescribed ocean-replicating conditions. The design of the EEL prototype evolved with modeling and simulation as well as early inferences about the stiffness of the tail body. Upon modification, it was found that the EEL design responded favorably to the proposed test conditions.

It was found from time-averaged simulations that, for station-keeping purposes, a large wave amplitude of 1.60 m and a wave period of 3 s provided the maximum lateral thrust to the EEL prototype in a horizontal orientation. The vertical orientation was found to produce less favorable thrust values. For passive gliding scenarios, it was found that ambient flow of 10 ft/s produced the desired lock-in condition required for long-term energy harvesting. Furthermore, it was observed that at 10 ft/s, the heavier mass of the prototype produced a larger height of oscillations. The addition of stored electrical energy back to the EEL prototype will be explored as active propulsion in future work.

REFERENCES

1. Leonard, B.P. "The ULTIMATE conservative difference scheme applied to unsteady one-dimensional advection". Comp. Meth. in Appl. Mech. and Eng., 1991, Vol. 88, p. 17–74.

2. Muzaferija, S. and Peric, M. 1999. "Computation of free surface flows using interface-tracking and interface-capturing methods", Chap. 2 in O. Mahrenholtz and M. Markiewicz (eds.), Nonlinear Water Wave Interaction, Computational Mechanics Publications, WIT Press, Southampton.

3. Shih, T.-H., Liou, W.W., Shabbir, A., Yang, Z. and Zhu, J. 1994. "A New k-ε Eddy Viscosity Model for High Reynolds Number Turbulent Flows – Model Development and Validation", NASA TM 106721.

4. Yang, B., Kaidi, S, and Lefrançois, E. "CFD Method to Study Hydrodynamics Forces Acting on Ship Navigating in Confined Curved Channels with Current". J. Mar. Sci. Eng. 2022, 10, 1263. https://doi.org/10.3390/jmse10091263.

5. N., & Mittal, S. (2016). Lock-in in vortex-induced vibration. Journal of Fluid Mechanics, 794, 565-594. doi:10.1017/jfm.2016.157